Strong influence of nonmagnetic ligands on the momentum-dependent spin splitting in antiferromagnets

Lin-Ding Yuan [●],[1] Zhi Wang,[1,2] Jun-Wei Luo,[2] and Alex Zunger [●][1,*]

[1]*Sustainable and Renewable Energy Institute, University of Colorado, Boulder, Colorado 80309, USA*
[2]*State Key Laboratory for Superlattices and Microstructures, Institute of Semiconductors,*
Chinese Academy of Sciences, Beijing 100083, China

Recent studies show the nonrelativistic antiferromagnetic ordering could generate momentum-dependent spin splitting analogous to the Rashba effect but free from the requirement of relativistic spin-orbit coupling. Whereas the classification of such compounds can be illustrated by different spin-splitting prototypes (SSTs) from symmetry analysis and density-functional-theory calculations, the huge variation in chemical bonding and structures of these diverse compounds possibly clouds the issue of how much of the variation in spin splitting can be traced back to the symmetry-defined characteristics, rather to the underlining chemical and structural diversity. The alternative model Hamiltonian approaches do not confront the issues of chemical and structural complexity but often consider only the magnetic sublattice, dealing with the all-important effects of the nonmagnetic ligands via renormalizing the interactions between the magnetic sites. To this end, we constructed a *DFT model Hamiltonian* that allows us to study SSTs at *constant chemistry* while retaining the realistic atomic-scale structure including ligands. This is accomplished by using a single, *universal* magnetic skeletal lattice (Ni^{2+} ions in rocksalt NiO) and designing small displacements of the nonmagnetic (oxygen) sublattice which produce, by design, the different SST magnetic symmetries. We show that (i) even similar crystal structures having very similar band structures can lead to contrasting behavior of spin splitting vs momentum, and (ii) even subtle deformations of the nonmagnetic ligand sublattice could cause a giant spin splitting in AFM-induced SST. This is a paradigm shift relative to the convention of modeling magnets without considering the nonmagnetic ligand that mediates indirect magnetic interaction (e.g., superexchange).

I. INTRODUCTION

The splitting of electronic states into spin bands has long been the focus of spin electronics [1–3] in either of the two approaches: (1) obtaining spin splitting as a result of the Zeeman effect via applied external magnetic fields or via the internal magnetic field of a ferromagnet [4], and (2) obtaining spin splitting in noncentrosymmetric systems via spin-orbit coupling (SOC) such as the Rashba [5] and Dressel-haus [6] effects. A third mechanism of momentum-dependent spin splitting, envisioned by Pekar and Rashba in 1964 to arise from the inhomogeneous magnetic field $h(\boldsymbol{r})$ in magnets [7], was noted recently in some antiferromagnets (AFMs) [8–10] and subsequently investigated microscopically by the present authors and Rashba [11] on the basis of atomic-scale electronic structure and magnetic symmetry [11,12]. Such SOC-unrelated (i.e., nonrelativistic) AFM-induced spin-splitting and polarization effects have been noted via density functional calculations by Ahn *et al.* [8] in the metallic collinear antiferromagnet rutile RuO_2 and has been attributed to the specific spin geometry in RuO_2, i.e., the two magnetic sublattices are related by a rotation of an angle $\pi/2$. Also, using the tight-binding calculation, Naka *et al.* [9] noted spin

splitting in a class of organic antiferromagnets compounds κ-$(BETD-TTF)_2Cu[N(CN)_2]Cl$ and suggested that the effect originates from the structural anisotropy associated with the checker-plate-type molecular arrangement in this compound. Using model Hamiltonians derived from multipole analysis, Hayami *et al.* studied the conditions enabling such nonrelativistic momentum-dependent spin-splitting effects in both collinear [10] and noncollinear antiferromagnets [13], and offered, based on the parameters of their model, Hamiltonian projection of other such cases [14].

A general method of magnetic symmetry analysis has been employed by Yuan *et al.* [11,12], studying the physical basis of nonrelativistic momentum-dependent spin splitting. This indicates that only antiferromagnets obeying certain magnetic symmetries could enable this spin-splitting effect. This method of analysis and its incorporation into density functional theory (DFT) calculations [11,12] provide both symmetry-dependent and material-dependent perspectives on previous nonsystematic sightings of AFM spin splitting, pointing out how different magnetic space groups (MSGs) can lead to seven distinct "spin-splitting prototypes" (SSTs). Using these derived symmetry rules, numerous compounds were identified in Ref. [12] as candidate AFM-induced spin splitting and sorted into different classes, some of which hold spin splitting even without SOC (i.e., nonrelativistic spin splitting), including both centrosymmetric and

*Corresponding author: alex.zunger@colorado.edu

noncentrosymmetric crystals. Such magnetic-symmetry-guided DFT calculations have been employed to illustrate the large AFM-induced spin-splitting effect in both collinear AFMs of rutile MnF_2 [11], orthorhombic $LaMnO_3$ [12], and rhombohedral $MnTiO_3$ [12], and noncollinear AFMs of cubic NiS_2 [12] and hexagonal $ScMnO_3$ [12]. The potential usefulness of this nonrelativistic origin of spin splitting relies in part on the fact that it can be realized also in compounds made of low-Z atoms and does not rely on the unstable chemical bonds (often leading to structural defects as in HgTe and Bi_2Se_3) of high-Z compounds that are required for large relativistic SOC in previous mechanisms.

These theoretical characterizations and microscopic explanations [7–12] of the underlying AFM spin-splitting effect have been followed by studies of their transport consequences [9,15–21]. This includes the calculation of the spontaneous Hall effect [15] in RuO_2 by Šmejkal et al., a compound noticed earlier by DFT calculations of Ahn *et al.* [8] to be an AFM spin-split system. Experimental realizations followed for RuO_2 [16], $SrRuO_3$ [17], and Mn_5Si_3 [18]. Also, the spin current generation effect was calculated using a tight-binding model by Naka *et al.* in a class of spin-split organic AFMs [9] and in the spin-split perovskites [19], and by González-Hernández *et al.* [20] in RuO_2 based on *ab initio* calculations. Building on the SOC-unrelated spin current generation in antiferromagnets, the giant and tunneling magnetoresistance was then calculated by Šmejkal *et al.* [21] in the stacked multilayer structures of RuO_2.

The current work is motivated by the observation that the identified compound realizations of nonrelativistic AFM spin splitting have widely different chemical bonding and crystal structures, possibly clouding the issue of how one can distinguish the contributions to spin splitting/polarization emerging from symmetry alone from the contributions due to chemical and structural variations. Previous calculations pointed to evidence on the importance of the nonmagnetic ligands. For example, the removal of F^- ions from the AFM MnF_2 changed it from a spin-splitting AFM to a no-spin-splitting AFM [11]; it was also noted that the rearrangement of the nonmagnetic oxygen atoms in the AFM RuO_2 [15] can reverse the crystal chirality and thus the accompanied spin splitting and the anomalous Hall effect. Our current approach to study different spin-splitting types at *constant chemistry* is to fix the chemical identity and geometry of the magnetic ions (here, Ni in NiO) and apply subtle positional changes to the nonmagnetic ligands (here, oxygen) so that the net increase in total energy is small (i.e., less than 30 meV/atom). This approach corresponds effectively to a DFT model Hamiltonian that allows us to study *spin-splitting prototypes* at constant chemistry while retaining the realistic atomic-scale structure including ligands.

Our DFT results show that (i) similar structures of NiO having different magnetic symmetries would enable or disable different mechanisms of spin splitting (no spin splitting, Zeeman splitting, AFM-induced splitting, and SOC-induced splitting); (ii) the profile of spin splitting vs momentum is determined not only by the position of the magnetic ions, but also by the positions of the nonmagnetic ligands that mediate the indirect interactions between magnetic atoms, such as superexchange [22] and double exchange [23]. Significantly, a

giant nonrelativistic AFM-induced spin splitting (~200 meV) emerges by a very small deformation (~0.04 Å) from its no-spin-splitting ground-state position. These insights on the role of nonmagnetic ligands are consequential for the fundamental understanding of magnetism [24,25] because of the large number of magnetic compounds outside elemental magnets and their intermetallic alloys that owe their chemical stability to the existence of bridging ligands. This opens new avenues in the research of perovskitelike multiferroic metal-organic-frameworks [26–28] where ligands are not simply atoms but organic ligands, offering a great number of opportunities for exploring the different organic ligands, different combinations of displacement patterns localized on the ligands, and even rotational degrees of freedom.

II. MODELING DIFFERENT SPIN-SPLITTING PROTOTYPES BY APPLYING SMALL DEFORMATIONS TO THE ROCKSALT AFM NiO

A. The unperturbed ground-state rocksalt NiO is an antiferromagnetic structure with no spin splitting

NiO is a wide-gap antiferromagnetic insulator below the Néel temperature (523 K) [29]. The spontaneous antiferromagnetic ordering in NiO originates from the superexchange interaction between Ni via the nonmagnetic oxygen *p* orbitals, as proposed by Anderson [22]. Such antiferromagnetic order creates inequivalence between the Ni atoms of neighboring (111) layers [denoted as Ni_α and Ni_β in Fig. 1(a)] and hence doubles the unit cell (two formula units per magnetic unit cell). Satoshi *et al.* synthesized the crystal using the Bernoulli method and determined the crystal structure via x-ray diffraction, achieving a good fit (R factor = 1.6%) [30] to the cubic structure (Pearson symbol cF8) at room temperature with lattice constant $a = 4.178$ Å [30]. Below the Néel temperature, the cubic crystal is slightly contracted along the $\langle 111 \rangle$ direction to a rhombohedral unit cell [29], a deformation ignored here, as it changes neither the magnetic space group nor the spin-splitting prototype. The antiferromagnetic order in NiO measured by neutron diffraction [31] shows that the crystal has ferromagnetic (111) sheets that couple antiferromagnetically with the magnetic moment perpendicular to the propagation vector $k = (\frac{1}{2}, \frac{1}{2}, \frac{1}{2})$. We adopt the experimental magnetization for the DFT calculations where the magnetic moments are aligned parallel or antiparallel to the $[11\bar{2}]$ direction [32].

One needs to exercise some care in establishing the strict nonrelativistic origin of the AFM spin splitting. One might have thought, for example, that the presently used magnetization orientation in NiO (here $[11\bar{2}]$ rather than [111]) originates from the magnetic anisotropy, which has a relativistic origin, thus clouding the nonrelativistic origin for the AFM spin-splitting effect reported here. However, our symmetry analysis (Appendix A) shows that the spin-splitting prototypes are independent of the magnetization orientation for all collinear antiferromagnetic compounds. This means that the AFM spin-splitting effect obtained with the magnetic orientation $[11\bar{2}]$ rather than [111] is not a reflection of the underlining relativistic origin of the magnetic anisotropy. For $[11\bar{2}]$-oriented NiO, our nonrelativistic DFT calculations
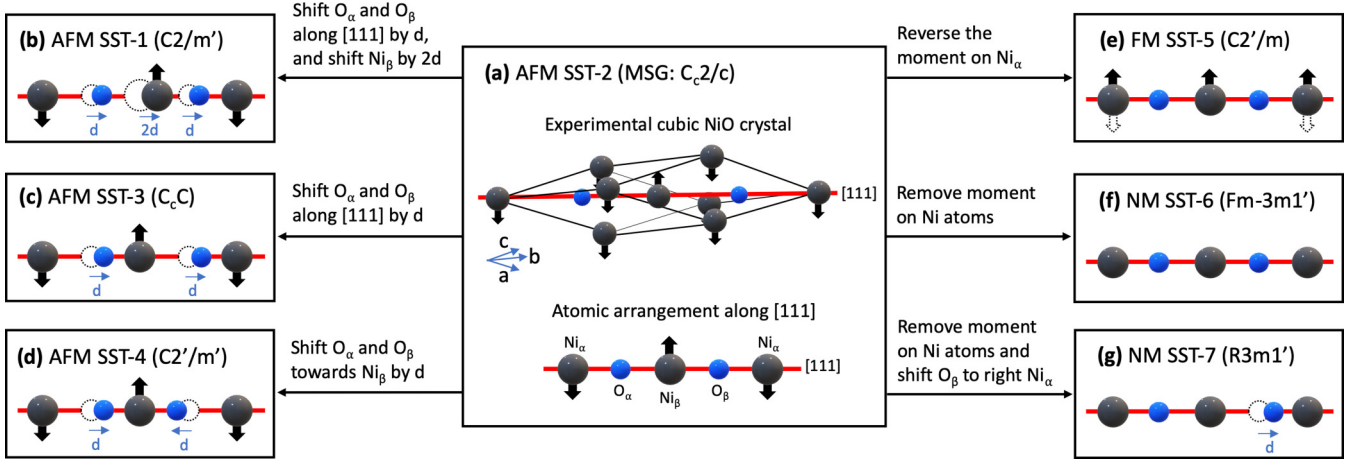
FIG. 1. Schematic diagrams of NiO atomic and magnetic structures for the seven spin-splitting prototypes. The models are uniquely represented by the atomic arrangement along the [111] direction (indicated by the red line) and the magnetic ordering on Ni (indicated by black arrows) in the unit cell. Here we have used the observed magnetization direction $[11\bar{2}]$. Ni_{α} and Ni_{β} (black circles) are the two Ni sites, and O_{α} and O_{β} (blue circles) are the two oxygen sites. Open and solid circles indicate, respectively, atomic positions before and after displacements d. (a) The experimentally observed AFM cubic phase of NiO belongs to spin-splitting prototype 2 (SST-2). The other six prototypes (b)–(g) are derived from the AFM rocksalt NiO experimental magnetic structure (AFM SST-2) by local distortions and flip/removal of magnetic moments.

(even assuming the [001] direction of magnetization) agree with the symmetry-based prediction and therefore can unambiguously suggest the right relativistic or nonrelativistic origin.

Another possible concern in establishing the nonrelativistic source of the AFM spin splitting is that in the distorted NiO models, the potential development of a secondary magnetic order corresponds to a canting of local magnetic moments away from collinearity and can be traced back to a relativistic origin, which might also cloud the nonrelativistic origin for the AFM spin-splitting effect. In fact, our DFT results show in the nonrelativistic spin-split AFM NiO structures that the relaxed magnetic moments indeed develop a secondary ferromagnetization on top of the assumed primary antiferromagnetic order. However, the secondary ferromagnetic moment is found to be very weak (less than 0.005 μ_{B}) and therefore has a negligible effect on the resulting spin splitting and has been ignored in our analysis. Since the spin splitting induced by (i) the primary antiferromagnetic order is dominant and immune to (i.e., unlikely to be manipulated by) the external magnetic field while the spin splitting induced by (ii) the secondary ferromagnetic order is smaller in magnitude and can be sensitively tuned by the external magnetic field, it is not hard to disentangle the contributions of the superposed spin splitting originating from (i) and (ii) in a measurement.

B. Gentle deformations of the NiO ground-state structure, converting it into other spin-splitting prototypes

The spin splitting of a magnetic compound is governed by its MSG symmetries, including both spatial symmetries (unitary part) and their combinations with time-reversal symmetry (antiunitary part). In general, MSG can be classified into four types: I, II, III, and IV [33–35]. MSG type I (colorless) has only spatial symmetries; MSG type II is the gray group, where for each spatial symmetry R in the group its combination

with time reversal ΘR is also in the group; MSG type III and type IV are known as *black-white* groups with an equivalent number of unitary symmetries and antiunitary symmetries. In MSG type III, the unitary part is related to the antiunitary part by an antirotation symmetry (combination of time reversal and rotation), while in MSG type IV, the unitary part is related to the antiunitary part by an antitranslation symmetry (combination of time reversal and a fractional lattice translation).

Our previous work [11,12] showed that the spin splitting of a magnetic compound is related to its MSG type as well as the presence or not of ΘIT symmetry. Formally, it can be summarized into two symmetry design principles (DPs) for nonrelativistic spin polarization and spin splitting: (DP-1) the absence of ΘIT symmetries, and (DP-2) the MSG being type I or type III. Violation of DP-1 then implies the presence of ΘIT symmetries; violation of DP-2 means that the MSG type is type II or IV. Depending on whether DP-1 and/or DP-2 are satisfied or violated, one can identify seven different spin-splitting prototypes [12]. The classification includes four AFM prototypes plus one ferromagnetic and two nonmagnetic prototypes.

To model all seven prototypes in the same stoichiometry, we use the ground-state NiO as the base structure and then search for small deformations that could tune the ground-state NiO into the other six different spin-splitting prototypes [12]. Such deformations, as shown in Fig. 1, include (i) atomic displacements off the rocksalt Wyckoff positions, and (ii) changes in the magnetic order (AFM, FM, and NM) via manipulations of local moments (by flipping or removing the spin moment). Note that our approach is to avoid the generation of a traditional model Hamiltonian (corresponding generally to omitting and including interaction terms at will, i.e., truncation) but rather to subtly manipulate atomic positions in a crystal that realizes new symmetries, and then act on these new structures by (untruncated) DFT, thus establishing their magnetic and spin properties.

a. SST-1 structure—Centrosymmetric MSG type III with ΘIT symmetry, showing no spin splitting. These are AFM compounds that violate DP-1 but satisfy DP-2. The violation of DP-1 then ensures no spin splitting for both SOC-off and SOC-on cases. The SST-1 NiO structure can be achieved by shifting the central Ni atom (Ni_β) off center by $2d$ (where d denotes the amplitude of displacement) and the two O atoms by d, all along the [111] direction [see Fig. 1(b)]. The resulting SST-1 structure has centrosymmetric parent space group R-3m and a magnetic space group of C2/m′ (MSG type III with ΘIT symmetry).

b. SST-2 structure—Centrosymmetric MSG type IV with ΘIT symmetry, showing no spin splitting. These are AFM compounds that violate both DP-1 and DP-2. The ground-state rocksalt AFM NiO [see Fig. 1(a)] is an example of SST-2, which has a centrosymmetric parent space group Fm-3m and magnetic space group of $C_c 2/c$ (MSG type IV with ΘIT symmetry).

c. SST-3 structure—MSG type IV without ΘIT symmetry, showing SOC-induced spin splitting in the presence of AFM. These are AFM compounds that satisfy DP-1 but violate DP-2. This allows spin splitting only when SOC is turned on but with AFM magnetization in the background. Such a magnetic background breaks the time-reversal symmetry and allows for spin splitting at TRIMs (see Appendix B for examples and detailed discussion). The SST-3 NiO structure can be achieved by shifting both O atoms along [111] by the same distance d while keeping the magnetic sublattices of Ni untouched [see Fig. 1(c)]. The resulting SST-3 structure has a noncentrosymmetric parent space group of R3m and a magnetic space group of $C_c c$ (MSG type IV without ΘIT).

d. SST-4 structure—MSG type III without ΘIT symmetry, showing AFM-induced spin splitting even without SOC. These are AFM compounds obeying both DP-1 and DP-2. Such spin splitting arises from AFM ordering (nonrelativistic effect); thus it can exist even with zero net magnetization and even when SOC is absent. The SST-4 NiO structure can be achieved by shifting the two oxygen atoms *towards* Ni_β by d while keeping the magnetic sublattices of Ni untouched [see Fig. 1(d)]. The resulting SST-4 structure has a centrosymmetric parent space group of R-3m and a magnetic space group of C2′/m′ (MSG type III without ΘIT). The forgoing condition of enabling nonrelativistic momentum-dependent spin-split antiferromagnets SST-4 [11,12] was later interpreted as "macroscopic time reversal symmetry breaking" in Ref. [18] and referred to as a "staggered Zeeman spin splitting antiferromagnet," a term not adopted here.

e. SST-5 structure—Ferromagnetic structure showing Zeeman-type spin splitting. These are ferromagnetic compounds that obey both DP-1 and DP-2. The resulting spin splitting is attributed to the Zeeman effect induced by the spontaneous net magnetization of the ferromagnet. The SST-5 NiO structure can be obtained by aligning the opposite and compensating magnetic moments of SST-2 on alternating (111) layers to the same direction, as shown in Fig. 1(e). The emergent nonzero net magnetization in this FM structure will then give rise to a Zeeman effect and split the spin-up and spin-down bands. The resulting FM SST-5 structure has a centrosymmetric parent space group of Fm-3m and a magnetic space group of C2′/m (MSG type III without ΘIT).

f. SST-6 structure—Centrosymmetric nonmagnets without spin splitting. These are nonmagnetic compounds that violate both DP-1 and DP-2. Like the CS AFM SST-1 and SST-2, the violation of DP-1 in SST-6 compounds then guarantees no spin splitting. The SST-6 NiO structure can be obtained by removing the local magnetic moments on all Ni [see Fig. 1(f)]. The resulting SST-6 structure has a centrosymmetric parent space group of Fm-3m and a magnetic space group of Fm-3m1′ (MSG type II with ΘIT).

g. SST-7 structure—Noncentrosymmetric nonmagnets, showing SOC-induced spin splitting as the Rashba-Dresselhaus effect. These are nonmagnetic structures satisfying DP-1 but violating DP-2. Such a spin-splitting effect occurs only when SOC is turned on, usually known as the Rashba [5] and Dresselhaus [6] effect. The SST-7 NiO structure can be obtained from SST-6 by further displacing one O atom along [111], which breaks the inversion symmetry [see Fig. 1(g)]. The resulting SST-7 structure has a noncentrosymmetric parent space group of R3m and a magnetic space group of R3m1′ (MSG type II without ΘIT).

III. ELECTRONIC STRUCTURE OF DIFFERENT SPIN-SPLITTING PROTOTYPES AT APPROXIMATELY CONSTANT CHEMISTRY

To simulate the electronic properties of the NiO structures, we employed DFT with the exchange-correlation functional of Perdew-Burke-Ernzerhof (PBE) [36,37]. The Dudarev method [38] is used, assigning an effective $U = 4.6$ eV [39] to account for the on-site Coulomb repulsion energy between Ni-3d electrons. The detailed computational settings are given in Appendix C.

A. Electronic property of undeformed rocksalt NiO (SST-2)

For ground-state NiO, we used the undeformed structure with an experimental lattice constant 4.178 Å [30] and antiferromagnetic ordering aligning along the [11$\bar{2}$] direction [40]. The calculated magnetic moment on Ni^{2+} ($3d^8$) is 1.7 μ_B comparable to the neutron-scattering results of 1.9 μ_B [40]. Electronic structure calculations show a direct gap at L of 3.55 eV and a smaller indirect gap of 2.98 eV between the valence-band maximum (VBM) at L and the conduction-band minimum (CBM) at some point on the Γ-K path (about 55% distant from Γ), which are smaller than the gap (4.3 eV) measured by combined photoemission/inverse photoemission [41].

B. Electronic properties of the seven different spin-splitting prototypes of NiO structures

The DFT-calculated electronic structures of the seven spin-splitting prototypes presented by NiO are depicted in Fig. 1 and summarized in Table I. It compares the parent space groups, the magnetic space groups, the magnetic moment vectors (a, a, -2a) on Ni, and the band gaps, with and without the SOC term in the Hamiltonian. For all NiO structures, the displacement parameter d is chosen to be 0.042 Å. Different sets of displacement parameter d do not change the underlining magnetic space-group symmetries but will affect the

TABLE I. Summary of DFT-calculated total energies, band gaps, magnetic moments, and maximal spin splitting, with and without SOC, for the seven NiO structures belonging to the seven spin-splitting prototypes (SST) (Fig. 1), together with their space groups and magnetic space groups. Noncollinear settings of magnetic moment oriented along $[11\bar{2}]$ are considered for both SOC off and SOC on. Maximum spin splitting is given for the top four valence bands and the bottom four conduction bands. For FM case SST-5, because of the difficulty in identifying pairs of spin-splitting states in the heavily entangled band structure, we provide spin-splitting values only by t he order of magnitude (>1 eV). DFT results are obtained using with the PBE exchange-correlation functional with $U = 4.6$ eV. Different structures are deformed from the experimental structure of NiO SST-2 with displacement parameter $d = 0.042$ Å, as shown in Fig. 1.

NiO structure prototypes:		AFM SST-1	AFM SST-2	AFM SST-3	AFM SST-4	FM SST-5	NM SST-6	NM SST-7
Spin-splitting consequence:		No spin splitting	No spin splitting	SOC	AFM	Zeeman	No spin splitting	Rashba-Dresselhaus
Parent space group:		R-3m	Fm-3m	R3m	R-3m	Fm-3m	Fm-3m	R3m
Magnetic space group:		C2/m′	C_c2/c	C_cC	C2′/m′	C2′/m	Fm-3m1′	R3m1′
Total energy (meV/fu)	SOC off	31	11	16	26	134	1678	1592
	SOC on	20	0	5	15	112	1662	1683
Magnetic moment	SOC off	0.682	0.682	0.682	0.682	0.723	0	0
(a, a, -2a) (μB)	SOC on	0.681	0.681	0.681	0.681	0.721	0	0
Band gap (eV)	SOC off	2.97	3.00	3.00	2.72	1.67	Gapless	Gapless
	SOC on	2.96	3.0	3.00	2.72	1.67	Gapless	Gapless
Max SS for top	SOC off	0.5	0	0	403.1	>1 eV	0	0
four VB (meV)	SOC on	0.7	0	60.6	403.1	>1 eV	0.0	45.0
Max SS for lowest	SOC off	0.3	0	0	285.0	>1 eV	0	0
four CB (meV)	SOC on	0.4	0	128.8	285.5	>1 eV	0.0	48.1

resulting spin splitting, which will also be discussed later in this section.

We note the changes in total energies relative to the ground-state SST-2 are very small for the four AFM spin-splitting prototypes (SST-1 to SST-4), because they differ with each other only by small displacements on oxygens. The resulting total DFT energies listed in Table I are given with respect to the undeformed rocksalt NiO (SST-2) with SOC, showing rather small destabilizations (less than 20 meV/formula unit). Removing SOC contributes to an additional small destabilization of approximately 11 meV. Moreover, the energy gaps and the magnetic moments of the four different AFM SSTs are similar (see Table I, rows 6 and 7) because (i) the atomic distortions are kept small and (ii) the SOC strength in NiO is negligible, since its constituent elements Ni ($Z = 28$) and O ($Z = 16$) are both rather low-Z elements. The other type of deformation (i.e., change of the magnetic order) would result in remarkable variations in properties. Specifically, the change from AFM (SST-2) to FM (SST-5) leads to a total energy increase by more than 100 meV/formula unit, a smaller band gap (1.67 eV), and a slightly larger magnetic moment on Ni sites (1.8 μB), while the change from AFM to NM (centrosymmetric SST-6 and noncentrosymmetric SST-7) leads to an enormous increase in energy ($\sim$1700 meV/formula unit), zero gap, and zero magnetic moment on Ni.

Despite the similarities in electronic and magnetic properties of AFM spin-splitting prototypes (SST-1 to SST-4), their spin-splitting consequences are distinct and differ greatly in the ensuring splitting amplitude. The last two rows of Table I give the maximum spin splitting for the top four valence bands (denoted as VB1, VB2, VB3, and VB4 in decreasing order of band energy) and the bottom four conduction bands (denoted as CB1, CB2, CB3, and CB4 in increasing order of band

energy), with and without SOC. We note three groups of spin-splitting consequences, which are consistent [12] with the SST classifications based on symmetry. (a) No spin splitting: AFM SST-1 and AFM SST-2, and centrosymmetric NM SST-6, all have zero spin splitting throughout the Brillouin zone for both with and without SOC (the small nonzero values below 1 meV of SST-1 are regarded as numerical errors in DFT calculations). (b) SOC-induced spin splitting: AFM SST-3 and non-centrosymmetric NM SST-7 both have nonzero spin splitting only when SOC is included in the Hamiltonian, and such spin splitting becomes zero when SOC is excluded, which therefore is referred to as SOC-induced spin splitting. (c) AFM-induced spin splitting: AFM SST-4 has a large momentum-dependent but SOC-unrelated spin splitting referred to as AFM induced. We were investigating whether the AFM spin-splitting manifests only on bands arising mostly from magnetic atoms or also from nonmagnetic ligands. On examination, we find for all AFM NiO structures that the valence band edge is composed of mostly O-p states mixed with small amounts of Ni-d states, while the conduction band edge is a roughly equal to hybridization of Ni-d states and O-p states.

Note again that the only difference among SST-2, SST-3, and SST-4 NiO structures is the oxygen displacement (Fig. 1), yet they show fundamentally different consequences on the spin splitting. Moreover, the AFM-induced spin splitting in SST-4 can take remarkable amplitudes of 403.1 meV (for VB1-4), much larger than the SOC-induced splitting in SST-3 (60.6 meV for VB1-4) or the conventional Rashba-Dresselhaus SOC-induced spin splitting in SST-7 (45 meV for VB1-4), the latter two as the common splitting amplitude in a weak SOC material (here, NiO).

To reveal the distinct physical origins of the SOC-induced spin-splitting structure (SST-3) and the AFM-induced
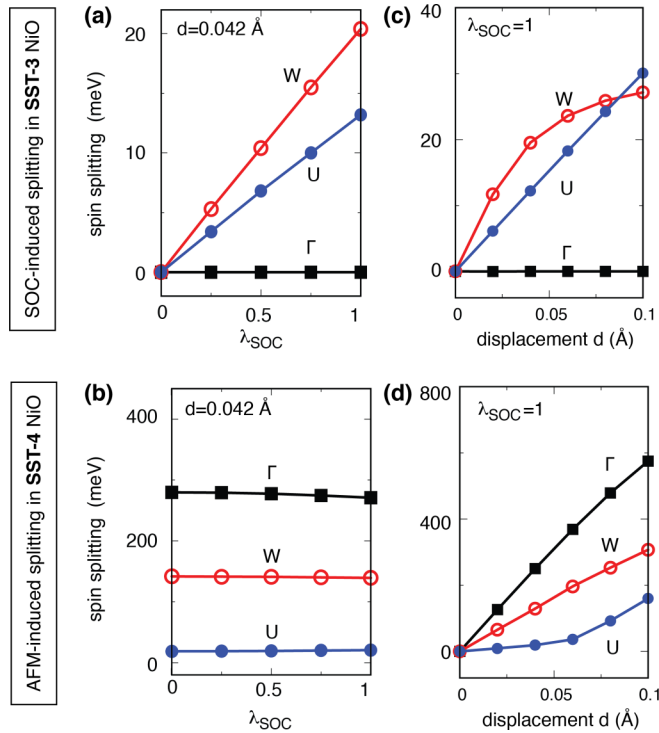
FIG. 2. Spin splitting of valence bands (the first spin pair) as a function of spin-orbit coupling strength λ_{soc} for (a) relativistic SOC-induced splitting in the presence of AFM (SST-3) and (b) nonrelativistic AFM-induced splitting (SST-4) using a fixed displacement $d = 0.042$ Å along [111] direction, and as a function of displacement d for (c) relativistic SOC-induced splitting in the presence of AFM (SST-3) and (b) nonrelativistic AFM-induced splitting (SST-4) with fixed SOC strength $\lambda_{SOC} = 1$.

spin-splitting structure (SST-4), we introduce a scaling factor λ_{soc} ($0 < \lambda_{SOC} < 1$) to the spin-orbit Hamiltonian term $H_{SOC} = \frac{\hbar}{2m_e^2 c^2} \frac{K(r)}{r} \frac{dV(r)}{dr} \hat{L} \cdot \hat{S}$ in the DFT formalism [42], where $\hat{L} = \hat{r} \times \hat{p}$ is the orbital angular momentum operator, $\hat{S}$ is the spin operator, $V(r)$ is the spherical part of the effective all-electron potential within the projector augmented plane-wave (PAW) sphere, and $K(r) = (1 - \frac{V(r)}{2m_e c^2})^{-2}$. By controlling the scaling factor λ_{soc}, we are then able to tune the strength of the SOC.

Figure 2 shows the spin splitting of spin pair 1 (VB1 and the next valence state with opposite spin polarization, which can be VB2, VB3, or the lower valence band) as a function of the scaling factor λ_{soc} for both SST-3 and SST-4. The identification of the spin pairs sometimes is not straightforward, as the assignment of members of the spin pair may change from one k point to another due to possible band crossing and anticrossing. In practice, for each k point we search for spin states with opposite signs of spin polarization (projecting on magnetization direction [11$\bar{2}$]), from VB1 downwards and CB1 upwards (see Appendix D for details of how to identify spin pairs). As evidenced in Fig. 2(a), the SOC-induced spin splittings of SST-3 AFM NiO at both W and U have a relativistic origin (linear to λ_{soc}) and become constantly zero at the Γ point, as enforced by the persisting ΘT symmetry in SST-3. In contrast, as shown in Fig. 2(b), the AFM-induced spin splitting in SST-4 NiO is an order of magnitude larger

than that of SST-3 (at W and Γ). Significantly, the resulting spin splittings are insensitive to SOC strength, suggesting their nonrelativistic origin.

We have shown how small distortions in the nonmagnetic oxygen atom position results in surprisingly fundamental changes in spin-splitting consequences for different SSTs. To see if such dependence of spin splitting to ligands is also consistent for the same SST, we examine the amplitudes of spin splitting for the SST-3 and SST-4 NiO structures as we continuously shift the oxygen (increase in d).

Figures 2(c) and 2(d) illustrate the spin splitting in SST-3 and SST-4 as a function of displacement d for spin pair 1. Clearly, the relation of spin splitting to oxygen displacement d strongly depends on what SST the structure belongs to. In SST-3 [Fig. 2(c)], the dependence of SOC-induced spin splitting on d is weak at all three k points. The splitting vs d relation is quadratic at W, but linear at Γ and U. While in AFM-induced SST-4, the dependence of AFM-induced spin splitting on d is much stronger and rather linear at the Γ and W points while being quadratic at U. We see that such nonrelativistic AFM-induced splitting is very sensitive to the deformation, as a small increase of displacement (from 0.0 to 0.1 A) could result in a remarkable rise of 200–600 meV in spin splitting.

C. Spin-polarized band structure and spin-splitting dispersion of individual prototypes

As noted in Fig. 2, for each SST the spin-splitting behavior can be different at different k points. We calculate the spin-splitting dispersion along certain high-symmetry k paths for all NiO structures. We focus on the spin splitting of the top four valence bands, as they are separated in energy from the other bands and thus free from the complex problem of bands entangling.

Figure 3 shows the spin-polarized band structures and dispersions of spin splitting of the four AFM prototypes (SST-1 to SST-4). Each prototype has two panels: the band structures of SOC off (left panel) and SOC on (right panel). For SST-3 and SST-4, the classification of centrosymmetric vs noncentrosymmetric divides these two prototypes further into four sub prototypes (two for each): SST-3A and SST-4A being centrosymmetric, SST-3B and SST-4B being noncentrosymmetric. Here, only one of the two subprototypes of SST-3 (3A and 3B) and SST-4 (4A and 4B) are shown, precisely being SST-3B (noncentrosymmetric) and SST-4A (centrosymmetric). In Fig. 3, for k points where the spin polarizations of bands are very close to zero, the definition of spin pair and spin splitting can be uncertain; we use gray patches with no data points to indicate such rare k paths. As discussed in Table I, the SS consequences of these AFM SSTs can be separated into three groups:

h. a. Prototypes having no spin splitting, either with or without SOC (SST-1, SST-2). The bands of centrosymmetric AFM SST-1 and SST-2 without SOC show similar dispersion but differ in band crossing and anticrossing on L-U and L-K (indicated by red and green circles), whereas adding SOC enables coupling between opposite spin states, therefore changing all crossing band to anticrossing as noticed on Γ-X, L-U, and L-K. The corresponding spin splitting is all zero with
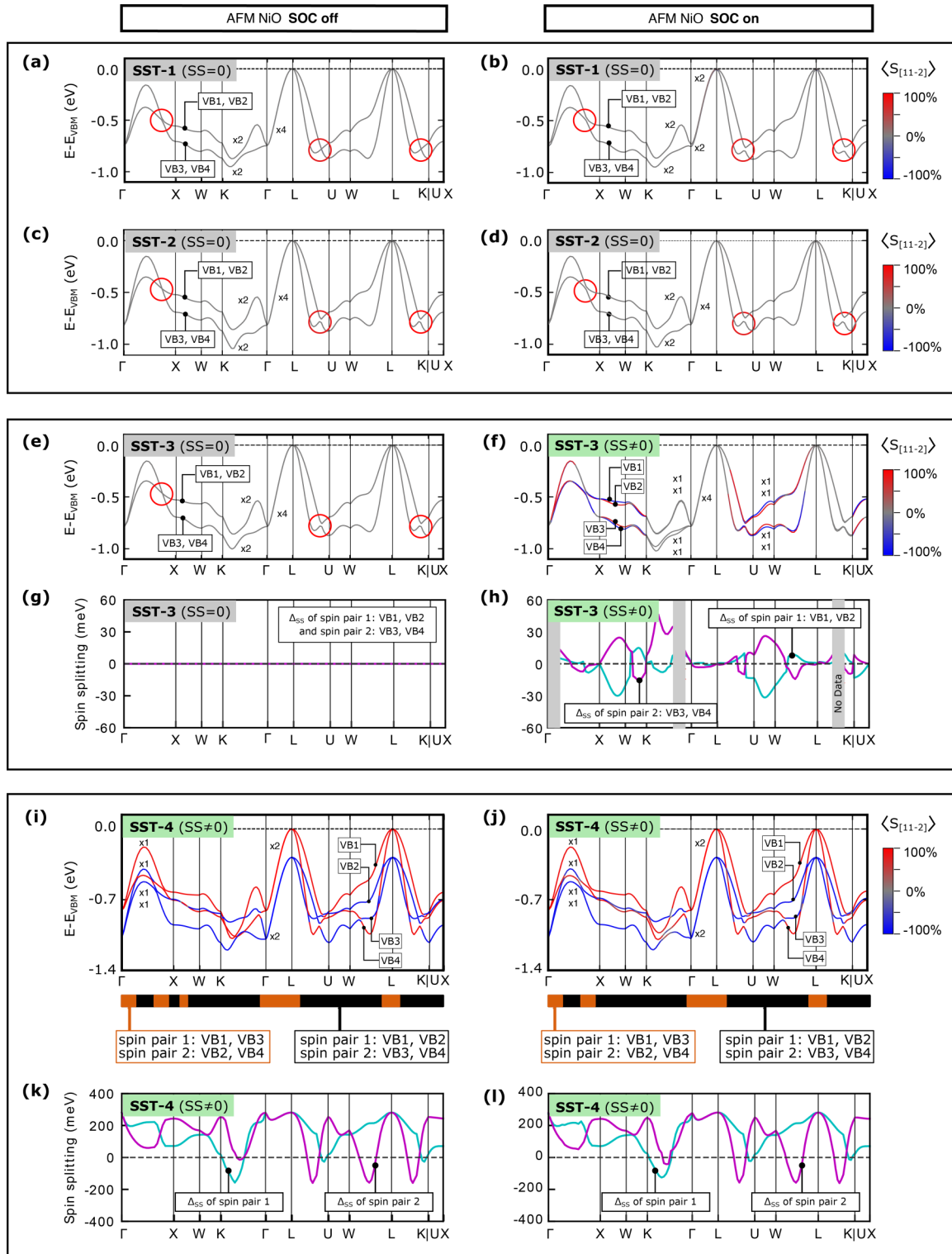
FIG. 3. DFT-calculated spin-polarized band structures and spin splitting of the top four valence bands in AFM NiO prototypes (SSTs) defined in Fig.1: (a), (b) for SST-1 (no-spin-splitting case) with SOC off (a) and SOC on (b); (c), (d) for SST-2 (no-spin-splitting case) with SOC off (c) and SOC on (d); (e), (f), (g), (h) for SST-3 (SOC-induced spin-splitting case) of the four spin-polarized bands with SOC off (e) and SOC on (f); and the spin splitting with SOC off (g) and SOC on (h); and (i), (j), (k), (l) SST-4 (AFM-induced spin splitting) of the four spin-polarized bands with SOC off (i) and SOC on (j); and the spin splitting with SOC off (k) and SOC on (l). The top four valence bands of NiO prototypes are labeled in the order of decreasing band energy as VB1, VB2, VB3, and VB4, regardless of band crossing or anticrossing (red circles). These bands are grouped into two spin pairs (1 and 2) of neighboring bands with opposite spin polarization (see Appendix D for details). The grouping can be either spin pair 1 consisting of VB1 and VB2 and spin pair 2 consisting of VB3 and VB4, indicated by black regions in panels (k) and (l), or spin pair 1 consisting of VB1 and VB3 and spin pair 2 consisting of VB2 and VB4, indicated by orange regions in panels (k) and (l). The color bars on the right-hand side provide the spin projection on the magnetization direction [11$\bar{2}$].

vanishing spin polarization, as mapped by the gray line color in the spin-polarized band plots in Figs. 3(a)–3(d).

b. Prototypes that have spin splitting only when SOC is present (SST-3). The SOC-induced splitting AFM SST-3 without SOC shows fully degenerate bands. It shares the same topology of degeneracies with SST-2 (no-spin-splitting AFM prototype) for the top four valence bands but differs from the latter in band crossing and anticrossing on L-U and L-K (indicated by circles). Adding SOC lifts the degeneracy in AFM SST-3. Such SOC-induced spin splitting has been mapped in Fig. 3(f) on high-symmetry k paths such as X-W-K and U-W-L, with red/blue showing the spin-up/spin-down polarized bands. The spin-splitting dispersion of $\boldsymbol{k}$ in Figs. 3(g) and 3(h) shows that such SOC-induced spin splitting (purple for the splitting of the first spin pair, and blue for the splitting of the second spin pair) in AFM SST-3 is relatively small in magnitude (<60 meV), reflecting the weak SOC strength in NiO.

c. Prototypes that have spin splitting regardless of SOC (SST-4). The bands of AFM SST-4 without SOC show similar dispersion and effective mass to other AFM spin-splitting prototypes SST-1 (no splitting), SST-2 (no splitting), and SST-3 (SOC-induced splitting) but show unique features of well-separated branches of spin-up and spin-down bands (identified by the spin projection on the magnetization direction [11$\bar{2}$]; see the color bars on the right-hand side of Fig. 3), whereas adding SOC contributes to only small changes in band structure (again, noticed as the change from crossing to anticrossing between opposite spin bands). We find that the AFM-induced spin splitting, which exists even when SOC is off [see Fig. 3(i)], is ~200 meV in magnitude, which is much larger than the SOC-induced splitting in SST-3 structure (<60 meV). Such large spin splitting is presumably attributed to the strong local magnetic moment on Ni sites.

In addition to the four AFM SSTs there are FM SST-5, NM SST-6 (centrosymmetric), and NM SST-7 (noncentrosymmetric):

d. Zeeman splitting in ferromagnets (SST-5). For SST-5, the undeformed rocksalt crystal but with a parallel FM ordering in the direction of [11$\bar{2}$] is used for the calculation. The DFT results [Fig. 4(a)] show a direct gap at Γ of 1.66 eV and a magnetic moment on Ni of 1.8 μ_B, which is slightly larger than the AFM magnetic moment. Because of the difficulty in identifying pairs of spin-splitting states in the heavily entangled band structure, the spin splitting is not evaluated to a number but shown by the nondegenerate spin-projected density of states (DOS) of up and down spins (identified by the spin projection on the magnetization direction [11$\bar{2}$]). The separated spin-up and spin-down DOSs seen in Fig. 4 for SOC off imply spin splitting in the FM SST-5 presence, even when SOC is off. Different from AFM SST-4, which also shows SOC-unrelated spin splitting, the spin splitting in FM arises from a different mechanism known as the Zeeman effect due to the nonzero net magnetization, the latter of which has a larger magnitude of ~1 eV.

e. No spin splitting in centrosymmetric NM SST-6 and SOC-induced (Rashba-Dresselhaus) spin splitting in noncentrosymmetric NM SST-7. Because of the removal of local magnetic moments, Ni^{2+} ions (3d^8) will have fully occupied t_{2g} orbitals (six electrons for six degenerated orbitals) but

(a) FM Zeeman induced SST-5 (SOC off)
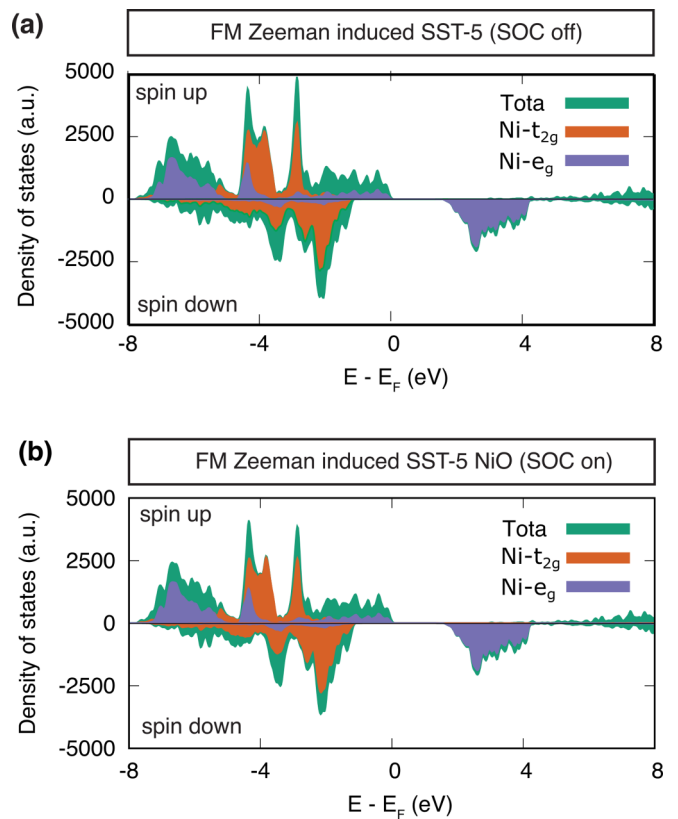
(b) FM Zeeman induced SST-5 NiO (SOC on)

FIG. 4. DFT results of spin and orbital-projected density of states showing Zeeman splitting in FM SST-5. The spin-projected (up and down; identified by the spin projection on the magnetization direction [11$\bar{2}$]) and orbital-projected (Ni-t_{2g} and Ni-e_g) density of states of FM SST-5 (a) when SOC is off and (b) when SOC is on.

only half-occupied e_g orbitals (two electrons for four degenerated orbitals); therefore the band gaps found in AFM and FM prototypes are close to zero in nonmagnetic prototypes (SST-6 and SST-7). For centrosymmetric NM SST-6, just like SST-1 and SST-2 (no spin-splitting AFM prototypes), the ΘIT symmetry is present and consequently ensures double spin degeneracy for every k point. This is evidenced by the spin-degenerate band with vanishing spin polarization shown in Fig. 5(a) and the corresponding zero spin splitting for spin pairs 1 and 2 shown in Fig. 5(b). In the noncentrosymmetric NM SST-7 [Figs. 5(c) and 5(d)], a small (<40 meV) spin splitting arises only when SOC is on. Such splitting has the same relativistic origin as the SOC-induced spin splitting in AFM SST-3, except that the latter has AFM order present.

IV. CONCLUSIONS

In this work we focus on the role of nonmagnetic ligands by examining systems of different spin-splitting prototypes at "constant chemistry." In contrast with previous approaches that attempted to introduce the effect of ligands on the magnetic symmetry by scaling the contribution to the amplitude of exchange interactions without the presence of ligands in the Hamiltonian, we opt for the latter. Our approach is implemented via a set of subtle structural deformation and magnetic deformations (from AFM to FM and NM) derived
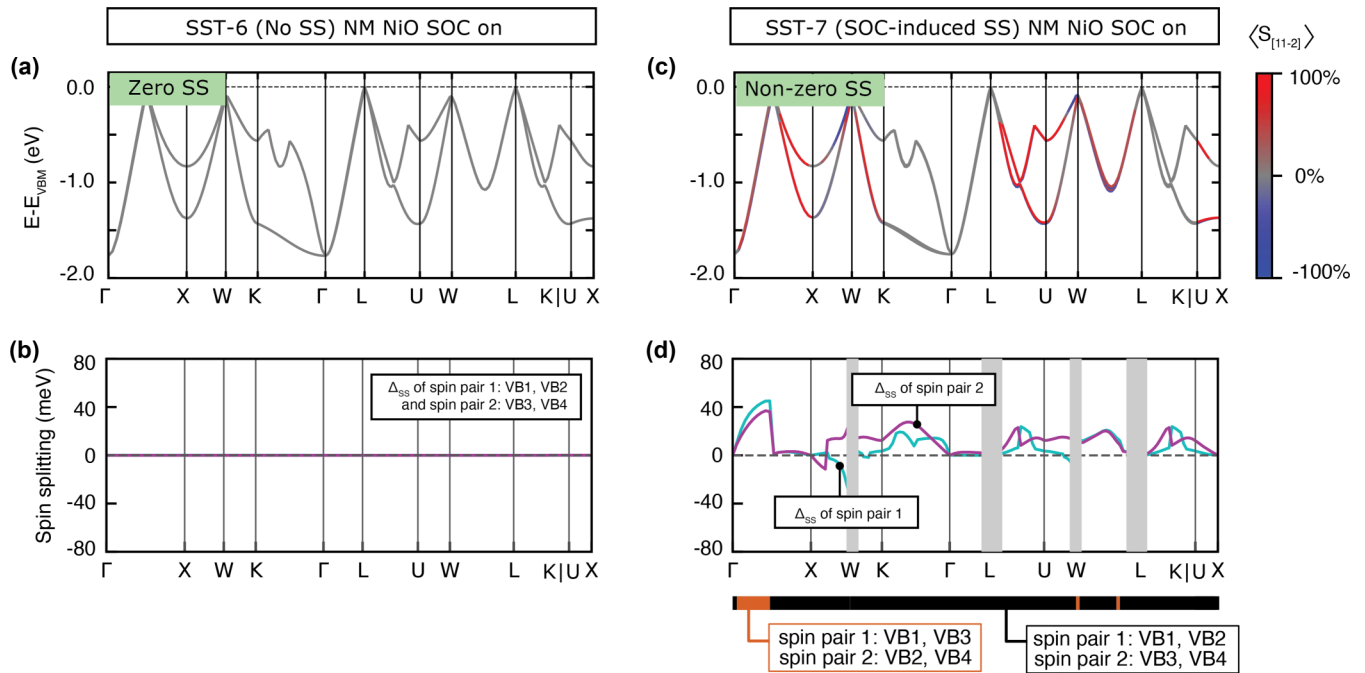
FIG. 5. Spin-polarized energy bands and spin splitting of the top four valence bands in nonmagnetic NiO prototype structures: (a) spin-polarized bands and (b) spin splitting for centrosymmetric SST-6 with SOC on; (c) spin-polarized bands and (d) spin splitting for noncentrosymmetric SST-7 with SOC on.

from one single base structure, the classic rocksalt AFM NiO [40], that each satisfies one of the seven spin-splitting symmetry conditions. To address the role of the often-neglected, nonmagnetic ligand atoms, the structural deformations are carefully designed to displace O atoms only while keeping Ni positions fixed. The first-principles DFT method has been used to study these seven designed structures of NiO.

Our main findings are as follows: (1) The profile of spin splitting vs momentum can be greatly affected by the Wyckoff position the nonmagnetic ions occupy. Rather similar structures of NiO, sharing the same magnetic sublattices but differing only by subtle deformations of the nonmagnetic ions, can have significantly different spin-splitting behaviors and significant differences in splitting amplitude. (2) We studied how the amplitude of spin splitting evolves with the deformation of oxygen in SST-3 and SST-4 NiO by showing a giant (~200 meV) nonrelativistic AFM-induced spin splitting in the slightly deformed SST-4 NiO (with only a small oxygen displacement of 0.04 Å from its original position in no-spin-splitting SST-2 NiO) in contrast to the small (~20 meV) SOC-induced spin splitting. We take the important role of the nonmagnetic ions as revealed in NiO structures as a serious warning to the tradition of considering only magnetic sublattices when modeling a magnet. We envision that the insights gained regarding the important role of the nonmagnetic ligand on momentum-dependent AFM spin splitting will motivate future exploration of more complex ligand effects. These might include organic ligands in the perovskitelike multiferroic metal-organic framework [26–28], with the different combinations of displacement, tilting patterns localized on the ligands that may influence the splitting of relevant band states, and other properties associated to the magnetic space-group symmetries.

APPENDIX A: COMPOUNDS OF DIFFERENT MAGNETIZATION ORIENTATIONS CAN HAVE DIFFERENT MAGNETIC SPACE GROUPS BUT BELONG TO THE SAME MSG TYPE AND THEREFORE THE SAME SPIN-SPLITTING PROTOTYPE

When SOC is on, the spatial rotation is also associated with the rotation of spin or local magnetic moment. The transformation of the magnetic moment under spatial rotation thus depends on the magnetization direction: (1) a π rotation around axes perpendicular to the magnetization orientation will reverse the on-site magnetic moment, but (2) a π rotation around axes parallel to the magnetization orientation

will keep the local magnetic moment unchanged. It opens the possibility for changing MSG via changing only the magnetization orientation. For example, the AFM NiO with [11$\bar{2}$]-oriented magnetic moments has MSG C_c2/c, while the AFM NiO with [1$\bar{1}$0]-oriented magnetic moments has a different MSG C_c2/m. In the former case, a π rotation around [1$\bar{1}$0] at center Ni$_\beta$ (denoted as $C_{2[1\bar{1}0]}$) keeps the atomic arrangement in the unit cell but reverses the magnetic moment on Ni atoms; therefore its combination with time reversal Θ (i.e., $\Theta C_{2[1\bar{1}0]}$) is a symmetry of its MSG C_c2/c; in the latter case, $C_{2[1\bar{1}0]}$ keeps the atomic arrangement in the unit cell and also keeps the orientation of magnetic moment on Ni atoms unchanged, thus $C_{2[1\bar{1}0]}$ (no need to combine with Θ) is a symmetry of MSG C_c2/m of the new model.

Although the change of magnetization orientation would change the MSG of a magnetic compound, it will not change the underlining MSG type or the presence or not of ΘIT symmetry. Therefore the change of magnetization orientation will not change the SST of an AFM compound. This conclusion is not limited to the NiO system but rather is general to all collinear antiferromagnetic compounds.

APPENDIX B: SPIN SPLITTING AT TIME-REVERSAL INVARIANT MOMENTS (TRIMs)

The k point that differs from $-k$ by a reciprocal lattice vector is known as a time-reversal invariant moment (TRIM). Typically, in a three-dimensional reciprocal space, the TRIMs are (0,0,0), (1/2,0,0), (0,1/2,0), (0,0,1/2), (1/2,1/2,0), (1/2,0,1/2), (0,1/2,1/2), and (1/2,1/2,1/2) in units of reciprocal lattices.

In nonmagnetic systems where the time-reversal symmetry is preserved, the time-reversal symmetry will also be a symmetry of the Hamiltonian at the TRIMs, hence guaranteeing a spin degeneracy and no spin splitting at the TRIMs. But unlike nonmagnetic systems, the AFM compounds violate the time-reversal symmetry Θ, thus allowing spin splitting to occur at the TRIM. However, this does not happen in SST-3 compounds where the MSG type is type IV, as the existence of an alternative symmetry, the ΘT symmetry, will again ensure spin degeneracy at TRIMs in the same manner as Θ for nonmagnets. The only AFM prototype that allows TRIM spin splitting is SST-4 (AFM-induced spin splitting). Such spin splitting on TRIMs is observed in the example of SST-4 NiO, where a spin splitting of approximately 200 meV is noticed [Figs. 3(i)–3(l)] at the Γ point. The formal method of determining TRIM degeneracy in magnetic systems requires the corepresentation theory and the use of the Herring theorem [43], as briefly described below.

Herring's theorem: In AFM compounds of a given MSG M, the degeneracies of the electronic states are determined by the irreducible corepresentation of M [44,45], which can be deduced from the irreducible representation of G. The dimension of the deduced corepresentation is two times the dimension of the irreducible representation. Whether such a corepresentation is irreducible (i.e., spin degeneracy) or reducible (i.e., spin splitting) can be achieved by the Herring

theorem [43]:

$$\sum_{B\in\{\Theta R_m\}} \chi^\Delta(B^2) = \begin{cases} g \; case\;(a) \\ 0 \; case\;(b) \\ -g \; case\;(c), \end{cases} \tag{B1}$$

where χ is the character of irreducible representation Δ of group G with index g. ΘR_m is an antiunitary symmetry of M with R_m representing a spatial symmetry. Case (a) corepresentation is reducible, meaning that the spin states having such corepresentation will split, while cases (b) and (c) corepresentations are both irreducible, i.e., spin degeneracy will be preserved. For example, every pair of spin states in MSG type-IV AFM holds either case (b) or (c) corepresentation and hence must be spin degenerate, because that for MSG type-IV AFM $\Theta T \in \{\Theta R_m\}$; thus it always has $\chi^\Delta((\Theta T)^2) = -1$ and hence cannot be case (a).

APPENDIX C: DENSITY FUNCTIONAL THEORY SETTINGS

The spin and electronic properties were calculated by the density functional theory (DFT) method with the Perdew-Burke-Ernzerhof (PBE) exchange-correlation functional [37], with $U = 4.6$ eV and $J = 0$ eV on Ni $3d$ orbitals [39] following the simplified rotationally invariant approach introduced by Dudarev *et al.* [38] implemented in the Vienna Ab initio Simulation Package (VASP). The atomic structures are either the experimental structure [46] or the deformed structures, changing only the internal atomic positions but keeping the experimental lattice vectors. To maintain the symmetry designed in Fig. 1, all atomic positions and lattice vectors are fixed and not allowed to change during DFT self-consistent iterations. The magnetic configurations of all magnetic NiO structures are simulated by initializing a starting magnetic configuration where magnetic moments take opposite direction on an alternating (111) Ni sheet and are collinearly aligned in the [11$\bar{2}$] direction. All magnetic moments are then allowed to relax during the DFT self-consistent iterations for electronic charge density. For every NiO structure, the MSG types obtained from the initial magnetic moments and the relaxed magnetic moments have been checked, and they are always identical. Note that in SST-4 NiO there exists in the finally relaxed magnetic moments a very weak secondary ferromagnetization on top of the assumed primary antiferromagnetic order, but such a secondary effect is very weak (less than 0.005 μ_B) and therefore has a negligible effect on the result spin splitting and has been ignored in the symmetry analysis. The nonmagnetic NiO structures are simulated by non-spin-polarized DFT calculations with the input parameter "ISPIN" set to 1 in VASP. For nonmagnetic NiO structures with SOC, the initial magnetizations on each atom are set to zero with "LSORBIT = .TRUE." in VASP and allowed to evolve during the DFT self-consistent iterations. The final magnetizations have been checked to be exactly zero, the structures are hence always nonmagnetic.

We adopt a plane-wave basis of up to 500-eV energy cutoff, a Γ-centered sampling of k-mesh $11 \times 11 \times 11$, and the tetrahedron smearing method for the calculations of a self-

consistent charge density. For all NiO structures, we chose the high-symmetry k paths from the conventional rhombohedral first Brillouin zone to show the band structures.

APPENDIX D: DETERMINING THE SPIN PAIRS

The assignment of the members of a spin pair can change from one k point to another due to band crossing and anticrossing (see red circles in Fig. 3). To solve this issue, we label the top four valence bands in decreasing order of band energy as VB1, VB2, VB3, and VB4. At every k point, the VB1-VB4 states can be grouped into two spin pairs (spin pairs 1 and 2) of neighboring bands with opposite spin polarization projected on the magnetization direction [11$\bar{2}$]. The two spin pairs can be either (a) spin pair 1 of VB1 and VB2 and spin pair 2 of VB3 and VB4, or (b) spin pair 1 of VB1 and VB3 and spin pair 2 of VB2 and VB4. For each spin pair the spin splitting takes a positive value when the up-spin state energy is higher than the down-spin state energy, and vice versa. However, not all k points have a clear definition for the spin pairs. The same procedure applies to determine spin-splitting pairs for other valence bands and conduction bands.

For states where the spin polarization is very close to zero, it is hard to determine whether the state is spin up or spin down due to the noncollinearity induced by SOC and the numerical errors. We use gray patches in Fig. 3 with no data points below it to indicate such rare k paths where the above definition of spin pairs is not applicable.

[1] S. A. Wolf, D. D. Awschalom, R. A. Buhrman, J. M. Daughton, S. v. Molnár, M. L. Roukes, A. Y. Chtchelkanova, and D. M. Treger, Spintronics: A spin-based electronics vision for the future, Science **294**, 1488 (2001).

[2] I. Žutić, J. Fabian, and S. D. Sarma, Spintronics: Fundamentals and applications, Rev. Mod. Phys. **76**, 323 (2004).

[3] A. Fert, The present and the future of spintronics, Thin Solid Films **517**, 2 (2008).

[4] P. Zeeman, The effect of magnetisation on the nature of light emitted by a substance, Nature (London) **55**, 347 (1897).

[5] E. Rashba and V. Sheka, Symmetry of energy bands in crystals of wurtzite type, II. Symmetry of bands with spin-orbit interaction included, Fiz. Tverd. Tela, Collected Papers (Leningrad) **2**, 162 (1959); published as the supplementary material to the article by Bihlmayer *et al.*, New. J. Phys. **17**, 050202 (2015).

[6] G. Dresselhaus, Spin-orbit coupling effects in zinc blende structures, Phys. Rev. **100**, 580 (1955).

[7] S. I. Pekar and E. I. Rashba, Combined resonance in crystals in inhomogeneous magnetic fields, Zh. Eksp. Teor. Fiz. **47**, 1927 (1964) [Sov. Phys. - JETP **20**, 1295 (1965)].

[8] K.-H. Ahn, A. Hariki, K.-W. Lee, and J. Kuneš, Antiferromagnetism in RuO_2 as d-wave Pomeranchuk instability, Phys. Rev. B **99**, 184432 (2019).

[9] M. Naka, S. Hayami, H. Kusunose, Y. Yanagi, Y. Motome, and H. Seo, Spin current generation in organic antiferromagnets, Nat. Commun. **10**, 4305 (2019).

[10] S. Hayami, Y. Yanagi, and H. Kusunose, Momentum-dependent spin splitting by collinear antiferromagnetic ordering, J. Phys. Soc. Jpn. **88**, 123702 (2019).

[11] L.-D. Yuan, Z. Wang, J.-W. Luo, E. I. Rashba, and A. Zunger, Giant momentum-dependent spin splitting in centrosymmetric low-Z antiferromagnets, arXiv:1912.12689 (2019); Giant momentum-dependent spin splitting in centrosymmetric low-Z antiferromagnets, Phys. Rev. B **102**, 014422 (2020).

[12] L.-D. Yuan, Z. Wang, J.-W. Luo, and A. Zunger, Prediction of low-Z collinear and noncollinear antiferromagnetic compounds having momentum-dependent spin splitting even without spin-orbit coupling, Phys. Rev. Mater. **5**, 014409 (2021).

[13] S. Hayami, Y. Yanagi, and H. Kusunose, Spontaneous antisymmetric spin splitting in noncollinear antiferromagnets without relying on atomic spin-orbit coupling, Phys. Rev. B **101**, 220403(R) (2020).

[14] S. Hayami, Y. Yanagi, and H. Kusunose, Bottom-up design of spin-split and reshaped electronic band structures in antiferromagnets without spin-orbit coupling: Procedure on the basis of augmented multipoles, Phys. Rev. B **102**, 144441 (2020).

[15] L. Šmejkal, R. González-Hernández, T. Jungwirth, and J. Sinova, Crystal Hall effect in Collinear Antiferromagnets, arXiv:1901.00445; Crystal time-reversal symmetry breaking and spontaneous Hall effect in collinear antiferromagnets, Sci. Adv. **6**, eaaz8809 (2020).

[16] Z. Feng, X. Zhou, L. Šmejkal, L. Wu, Z. Zhu, H. Guo, R. González-Hernández, X. Wang, H. Yan, P. Qin, X. Zhang, H. Wu, H. Chen, C. Jiang, M. Coey, J. Sinova, T. Jungwirth, and Z. Liu, Observation of the crystal Hall effect in a collinear antiferromagnet, arXiv:2002.08712.

[17] K. Samanta, M. Ležaić, M. Merte, F. Freimuth, S. Blügel, and Y. Mokrousov, Crystal Hall and crystal magneto-optical effect in thin films of $SrRuO_3$, J. Appl. Phys. **127**, 213904 (2020).

[18] R. L. S. Helena Reichlova, R. Gonzalez-Hernandez, I. Kounta, R. Schlitz, D. Kriegner, P. Ritzinger, M. Lammel, M. Leiviska, V. Petricek, P. Dolezal, E. Schmoranzerova, A. Badura, A. Thomas, V. Baltz, L. Michez, J. Sinova, S. T. B. Goennenwein, T. Jungwirth, and L. Semjkal, Macroscopic time reversal symmetry breaking by staggered spin-momentum interaction, arXiv:2012.15651.

[19] M. Naka, Y. Motome, and H. Seo, Perovskite as a spin current generator, Phys. Rev. B **103**, 125114 (2021).

[20] R. González-Hernández, L. Šmejkal, K. Výborný, Y. Yahagi, J. Sinova, T. Jungwirth, and J. Železný, Efficient Electrical Spin Splitter Based on Nonrelativistic Collinear Antiferromagnetism, Phys. Rev. Lett. **126**, 127701 (2021).

[21] A. B. H. Libor Šmejkal, R. González-Hernández, J. Sinova, and T. Jungwirth, Giant and tunneling magnetoresistance effects from anisotropic and valley-dependent spin-momentum interactions in antiferromagnets, arXiv:2103.12664.

[22] P. W. Anderson, Antiferromagnetism. Theory of superexchange interaction, Phys. Rev. **79**, 350 (1950).

[23] C. Zener, Interaction between the d-Shells in the transition metals. II. Ferromagnetic compounds of manganese with perovskite structure, Phys. Rev. **82**, 403 (1951).

[24] B. D. Cullity and C. D. Graham, *Introduction to Magnetic Materials* (John Wiley & Sons, New York, 2011).

[25] D. Jiles, *Introduction to Magnetism and Magnetic Materials* (CRC Press, Boca Raton, FL, 2015).

[26] A. Stroppa, P. Jain, P. Barone, M. Marsman, J. M. Perez-Mato, A. K. Cheetham, H. W. Kroto, and S. Picozzi, Electric control of magnetization and interplay between orbital ordering and ferroelectricity in a multiferroic metal-organic framework, Angew. Chem. Int. Ed. **50**, 5847 (2011).

[27] Z. Wang, P. Jain, K.-Y. Choi, J. van Tol, A. K. Cheetham, H. W. Kroto, H.-J. Koo, H. Zhou, J. Hwang, E. S. Choi, M.-H. Whangbo, and N. S. Dalal, Dimethylammonium copper formate $[(CH_3)_2NH_2]Cu(HCOO)_3$: A metal-organic framework with quasi-one-dimensional antiferromagnetism and magnetostriction, Phys. Rev. B **87**, 224406 (2013).

[28] F. Lou, T. Gu, J. Ji, J. Feng, H. Xiang, and A. Stroppa, Tunable spin textures in polar antiferromagnetic hybrid organic–inorganic perovskites by electric and magnetic fields, npj Comput. Mater. **6**, 114 (2020).

[29] H. Rooksby, A note on the structure of nickel oxide at subnormal and elevated temperatures, Acta Crystallogr. **1**, 226 (1948).

[30] S. Sasaki, K. Fujino, Eacute Tak, and Y. Uchi, X-Ray determination of electron-density distributions in oxides, MgO, MnO, CoO, and NiO, and atomic scattering factors of their constituent atoms, P. Japan Academy Ser. B **55**, 43 (1979).

[31] C. G. Shull, W. A. Strauser, and E. O. Wollan, Neutron diffraction by paramagnetic and antiferromagnetic substances, Phys. Rev. **83**, 333 (1951).

[32] J. Baruchel, M. Schlenker, K. Kurosawa, and S. Saito, Antiferromagnetic S-domains in NiO, Philos. Mag. B **43**, 853 (1981).

[33] A. M. Zamorzaev, Generalization of Fedorov groups, Ph.D. thesis, Leningrad University 1953; Kristallografiya **2**, 15 (1957) [Sov. Phys. Crystallogr. **2**, 10 (1957)].

[34] D.B. Litvin, *Magnetic Group Tables: 1-, 2- and 3-Dimensional Magnetic Subperiodic Groups and Magnetic Sapce Groups* (International Union of Crystallography, Chester, England, 2013).

[35] L. D. Landau, J. S. Bell, M. J. Kearsley, L. P. Pitaevskii, E. M. Lifshitz, and J. B. Sykes, *Electrodynamics of Continuous Media* (Oxford, Butterworth-Heinemann, 1984), Sec. V, Vol. 8.

[36] J. P. Perdew, K. Burke, and M. Ernzerhof, Generalized Gradient Approximation Made Simple, Phys. Rev. Lett. **77**, 3865 (1996).

[37] J. P. Perdew, J. A. Chevary, S. H. Vosko, K. A. Jackson, M. R. Pederson, D. J. Singh, and C. Fiolhais, Atoms, molecules, solids, and surfaces: Applications of the generalized gradient approximation for exchange and correlation, Phys. Rev. B **46**, 6671 (1992).

[38] S. L. Dudarev, G. A. Botton, S. Y. Savrasov, C. J. Humphreys, and A. P. Sutton, Electron-energy-loss spectra and the structural stability of nickel oxide: An LSDA+U study, Phys. Rev. B **57**, 1505 (1998).

[39] M. Cococcioni and S. de Gironcoli, Linear response approach to the calculation of the effective interaction parameters in the LDA+U method, Phys. Rev. B **71**, 035105 (2005).

[40] E. Ressouche, N. Kernavanois, L.-P. Regnault, and J.-Y. Henry, Magnetic structures of the metal monoxides NiO and CoO reinvestigated by spherical neutron polarimetry, Physica B **385**, 394 (2006).

[41] G. A. Sawatzky and J. W. Allen, Magnitude and Origin of the Band Gap in NiO, Phys. Rev. Lett. **53**, 2339 (1984).

[42] S. Steiner, S. Khmelevskyi, M. Marsmann, and G. Kresse, Calculation of the magnetic anisotropy with projected-augmented-wave methodology and the case study of disordered $Fe_{1-x}Co_x$ alloys, Phys. Rev. B **93**, 224425 (2016).

[43] C. Herring, Effect of time-reversal symmetry on energy bands of crystals, Phys. Rev. **52**, 361 (1937).

[44] J. O. Dimmock and R. G. Wheeler, Symmetry properties of wave functions in magnetic crystals, Phys. Rev. **127**, 391 (1962).

[45] R.-X. Zhang and C.-X. Liu, Topological magnetic crystalline insulators and corepresentation theory, Phys. Rev. B **91**, 115317 (2015).

[46] W. L. Roth, Magnetic structures of MnO, FeO, CoO, and NiO, Phys. Rev. **110**, 1333 (1958).